Low resistivity ZnO-GO electron transport layer based $CH_3NH_3PbI_3$ solar cells

Cite as: AIP Advances **6**, 065303 (2016); https://doi.org/10.1063/1.4953397
Submitted: 19 March 2016 • Accepted: 25 May 2016 • Published Online: 13 June 2016

Muhammad Imran Ahmed, Zakir Hussain, Mohammad Mujahid, et al.

Low resistivity ZnO-GO electron transport layer based $CH_3NH_3PbI_3$ solar cells

Muhammad Imran Ahmed,[1,a] Zakir Hussain,[1] Mohammad Mujahid,[1] Ahmed Nawaz Khan,[1] Syed Saad Javaid,[2] and Amir Habib[1,3,a]
[1]*School of Chemical and Materials Engineering, National University of Sciences and Technology, Islamabad, 44000, Pakistan*
[2]*College of Aeronautical Engineering, National University of Sciences and Technology, Islamabad, 44000, Pakistan*
[3]*The Department of Physics, College of Sciences, University of Hafar Al Batin, P.O. Box 1803, Hafar Al Batin 31991 Saudi Arabia*

(Received 19 March 2016; accepted 25 May 2016; published online 13 June 2016)

Perovskite based solar cells have demonstrated impressive performances. Controlled environment synthesis and expensive hole transport material impede their potential commercialization. We report ambient air synthesis of hole transport layer free devices using ZnO-GO as electron selective contacts. Solar cells fabricated with hole transport layer free architecture under ambient air conditions with ZnO as electron selective contact achieved an efficiency of 3.02%. We have demonstrated that by incorporating GO in ZnO matrix, low resistivity electron selective contacts, critical to improve the performance, can be achieved. We could achieve max efficiency of 4.52% with our completed devices for ZnO: GO composite. Impedance spectroscopy confirmed the decrease in series resistance and an increase in recombination resistance with inclusion of GO in ZnO matrix. Effect of temperature on completed devices was investigated by recording impedance spectra at 40 and 60 °C, providing indirect evidence of the performance of solar cells at elevated temperatures. [http://dx.doi.org/10.1063/1.4953397]

I. INTRODUCTION

From Kyoto to COP21, it has been two decades and we are increasingly becoming aware of the effect that fossil fuels have had on our environment. Sustainable development for the future needs renewable energy sources and the discovery of perovskite has been dubbed as the next big things in photovoltaics. Though the material has been around for quite some time, it was only recently that its photovoltaic performance was demonstrated. Form those initial reports, it has grown tremendously with each passing day on the back of intense research efforts with a certified efficiency of 20.1%.[1]

Properties too good to be true for photovoltaic performance; these materials have demonstrated all of them. Ambipolar charge transport, long diffusion lengths, low excitons binding energies, earth abundant materials and a facile solution processing are all the right ingredients for the next generation photovoltaic revolution.[2,3] Mesoporous,[4] mesosuperstructured[2] and planner geometries[5] have been investigated yielding comparable performances in each geometry. Scaffolds have evolved from TiO_2 to insulating Al_2O_3 and Zirconia.[6–8] Architectures have been investigated comprising both hole transport layers (HTL) and without HTL[9]; achieving impressive performance in later case too. Synthesis routes evolved from one step solution processing[10] to two step sequential deposition,[11]

[a]Authors to whom correspondence should be addressed. Electronic addresses: imranrahbar@scme.nust.edu.pk and amirhabib@scme.nust.edu.pk.

vapor assisted growth,[4] sublimation and an ever increasing mix. Synthesis has also been reported under ambient conditions of high humidity yielding an efficiency of 15%.[11]

TiO_2 being the material of choice for electron selective contact, ZnO as electron selective has also been explored with varying degree of success. ZnO a wide band gap semiconductor has superior charge transport properties over TiO_2. Developed in the back drop of DSSCs,[12,13] TiO_2 has been the most explored electron selective contact for perovskite solar cells. High optical transparency, charge carrier mobilities and superior charge transport properties of ZnO as well as extensive literature on ZnO based devices make this material a viable candidate for exploring as electron selective contact.[14–16]

Graphene, a wonder material, also offers new avenues in nano composites when combined with these wide band gap semiconductors. Excellent optical transparency, mechanical strength and electrical conductivity have lead to its use in numerous applications. Its chemical stability renders its use as nanocomposite with other materials. With its high optical transparency and specific surface area, it has been investigated with the aim of replacing indium based transparent conducting oxide, potentially opening way for flexible substrates.[17,18] TiO_2, Fe_3O_4 and ZnO have been investigated as nanocomposite with GO, offering properties superior to individual materials.[19–21] ZnO-GO composites have been reported for applications like corrosion protection, photocatalysis, batteries, field emission prosperities and for incorporation in polymer solar cells.[22–24]

Both graphene and reduced graphene oxide have been used as nanocomposite with TiO_2 in perovskite solar cells.[25,26] Incorporation of graphene is reported to have reduced the series resistance component of the solar cells resulting in increase in their efficiency. Therefore, graphene-ZnO nanocomposites could be potential materials to be further explored. ZnO has been doped with Al,[27] developed into nano rods[28] and employed as a bilayer with TiO_2.[29] However no report is available for incorporation of GO in ZnO for electron selective contact. We have incorporated this composite as electron selective contact in a hole transport layer free device geometry and tailored the fabrication protocol for ambient air conditions of high humidity.

Focus of the research being reported was to lower the cost of perovskite solar cells. Though perovskite being earth abundant, HTL most commonly used for high efficiency perovskite devices (Spiro-MeOTAD) is very expensive, put to a large scale cell for commercial application, the cost would be prohibitive. Another bottleneck is the requirement of controlled conditions such as high vacuum environment for processing. We set forth to achieve devices based on HTL free architecture while processing under ambient air conditions of high humidity. Though both techniques have separately been reported earlier, there is no report for HTL free device processing under ambient air conditions. We used ZnO as electron selective contact with $CH_3NH_3PbI_3$ absorber. Device parameters were evaluated and GO was incorporated to improve the performance of the devices; the best performing device efficiency achieved was 4.7%. To the best of our knowledge, it is the first report for HTL free ambient air synthesized $CH_3NH_3PbI_3$ solar cell using ZnO-GO composite as electron selective contact.

II. MATERIALS AND METHODS

All materials were sourced from Sigma Aldrich and were used without further purification. CH_3NH_3I (MAI) was purchase from Dyesol (MS101000-50). ZnO nano particles were synthesized through sol gel process. 0.2 M zinc acetate dihydrate ($Zn(CH_3COO)_2{\cdot}2H_2O$) solution in iso-propanol was stabilized with Monoethanolamine (MEA) $(HOCH_2CH_2)NH_2$ as stabilizer in the molar ratio MEA:Zn^{2+}[30] and the mixture was stirred to achieve clear solution as sol which was allowed to age for 24 hr before film formation. GO was synthesized by modified Hummer's method.[31] As prepared GO was dispersed in iso-propanol at 5 mg/ml and was ultrasonicated for 30 min. This dispersion was added to ZnO sol at various concentrations to obtain 0.2, 0.4, 0.6, 0.8 and 1 vol% of GO solution dispersion in ZnO sol. ZnO-GO composite was spin coated on pre cleaned ITO coated glass slides (resistivity 15 Ω/cm^2 10x10 cm^2) at 2000 rpm for 25 s, samples were then annealed in an oven for 10 min at 200 ^oC to decompose organic part before further film deposition. The process of ZnO deposition and intermediate annealing step was repeated 4 times to achieve a film thickness of 300 nm. Samples were then annealed in an oven at 400 ^oC for 2 hr with a heating

rate of 10 °C per min and were allowed to cool to room temperature in an oven. $CH_3NH_3PbI_3$ was synthesized under ambient conditions of high humidity. With certain changes in the already reported procedure[11] we could obtain uniform large area coverage of $CH_3NH_3PbI_3$ on ZnO-GO coated ITO glass slide. For the preparation of 1.0 M solution of PbI_2, repeated efforts failed to achieve complete dissolution of PbI_2 in DMF even after prolonged stirring at 100 °C. However, overnight vacuum drying at 100 °C and addition of few micro liters of hydro iodic acid resulted in complete dissolution of lead iodide in DMF. This solution was spin coated on preheated (50 °C) ZnO coated glass slides at 3000 rpm for 20 s. Lead iodide coated slides were oven dried at 40 °C for 3 min and at 100 °C for 5 min and were again mounted on the spin coater for wetting with MAI. Initial wetting with MAI with soaking time of 20 s resulted in non uniform coverage of the films, evident from the ring patterns as shown in Fig S1.[63] However, this problem was overcome by wetting the films with 20 µl of iso-propanol while it was spinning followed by the addition of MAI solution. Films obtained exhibited light brown texture and were again soaked in MAI solution in iso-propanol for 20 s followed by spin coating for 20 s at 3000 rpm and drying with hot air resulted in rapid crystallization. Coated films were oven dried at 40 °C for 3 min and 100 °C for 5 min. Finally, devices obtained were coated with 100 nm thick layer of gold by thermal evaporation using a metallic mask defining active area of the device as 0.9 cm^2. Thus the completed devices had architecture of ITO: ZnO: $CH_3NH_3PbI_3$: Au, with layer thicknesses of 100nm, 300 nm, 400 nm and 100 nm respectively.

III. CHARACTERIZATION

Film morphology was analyzed through Atomic Force Microscope (AFM) under ambient air conditions (JEOL SPM 5200, NSC35 micro fabricated cantilevers tip) and thermionic emission Scanning Electron Microscope (SEM) (JEOL JSM6490A). Structural analysis was performed through X-ray diffraction on STOE Stadi MP X-ray diffrectometer with a working voltage of 40KV and 20 mA current. Cu Kα source was used, measuring between 5 to 60 degrees in θ- 2θ mode. Film resistivity measurements were made using ECOPIA HMS-5000 Hall effect measuring apparatus employing silver paste to form reliable contacts on films. J-V characterization was done on Keithley 2400 source meter, using Newport 67005 solar simulator with AM 1.5G filter at an intensity of 100 mW/cm^2. Cyclic Voltammetery and Impedance spectroscopy studies were performed using Biologic electrochemical work station and the obtained data were analyzed using Biologic EC-Lab V10.40 software package. Cells were evaluated using a 20mV perturbation from a frequency range of 1 MHz to 500 mHz under illumination of 100 mW/ cm^2. Thickness measurements were obtained by Nanovia optical profilometer with data processing on mountain 2 D software suite by Nanovia.

IV. RESULTS AND DISCUSSION

As prepared GO was investigated for its quality. The XRD pattern presented in Fig. 1(a) shows peak shift from 26.47° of graphite (JCPDS Card No. 01-0640) to 11.8° indicating exfoliation of graphite flakes.[32] Honey comb structure of graphite is preserved in the exfoliated sheets evident from minor peak broadening.[33] Large area sheets of the order of tens of microns are visible in both SEM and AFM micrographs in Fig. 1(b), 1(c), indicating the quality of exfoliated graphene. AFM images were obtained by preparing GO dispersion over silicon wafers to guard against any roughness of glass slide interfering with the roughness prolife of GO. Roughness profile from AFM indicates sheet thickness of 0.4 to 1 nm in Z axis, a proof of obtaining single graphene sheets.

Study of ZnO GO composite under SEM and AFM (Fig. 2) reveals a uniform film formation with mean square roughness of 3.69 nm. Detailed study of the films under SEM (Fig. 2(a)-2(d)) revealed that few locations can be identified where GO sheets appear on the surface of the films, indicating that GO films have uniformly been imbedded in the particle matrix. Observation of sheets on the surface of ZnO films (Fig. 2(a), 2(b)) suggests the restacking of sheets against the finely dispersed sheets when GO dispersions are studied under AFM (Fig. 1(c)). This restacking is

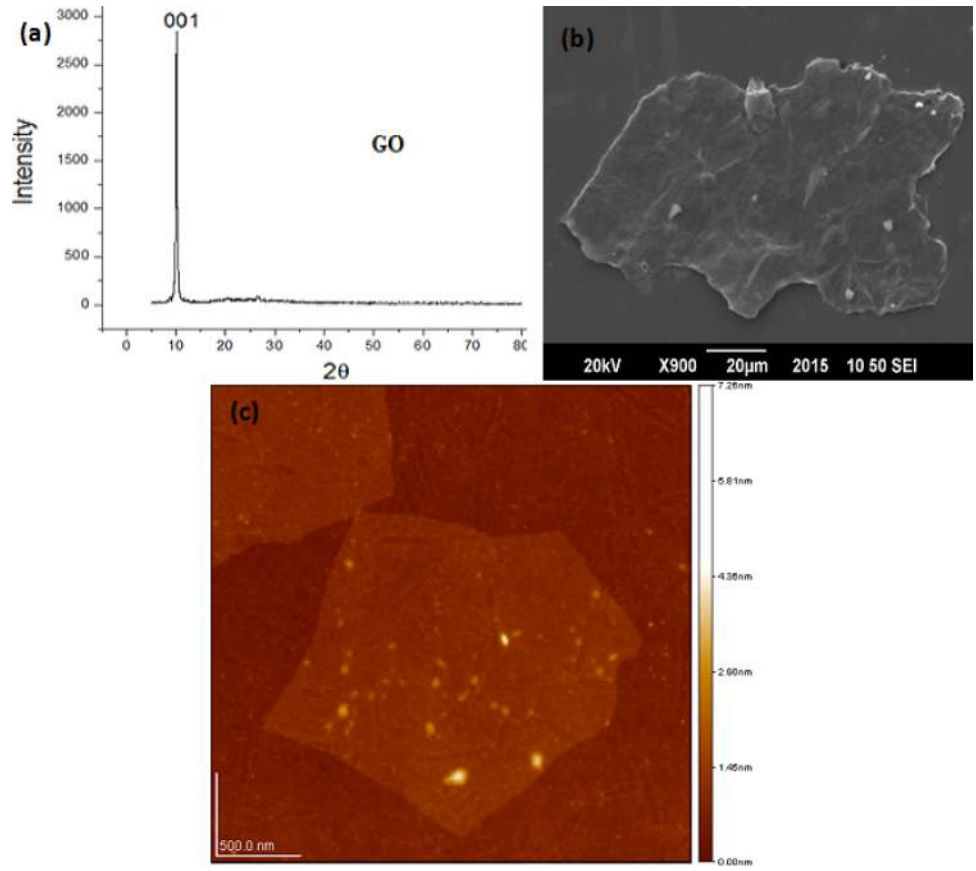

FIG. 1. (a) XRD pattern of GO powder, SEM (b) and AFM (c) images of GO dispersions.

observed in sol gel process and could be attributed to evaporation during annealing since solvents prevent staking of sheets by ensuring good dispersion.[34,35] Methods for avoiding this restacking have been proposed in the literature which involve e.g. introducing CNTs in sheets and controlled deposition of nanosheets.[36,37] Sheets appearing on the surface are also uniformly covered with ZnO particles and a fibrous network of wrinkles can be identified around GO sheets (Fig. 2(a), 2(b)). This network is associated with either lack of OH^- groups in the sol or the stress relaxation due to coefficient of thermal expansion mismatch. Since this network is observed only around GO sheets on the surface of the films, this is most likely due to stress relaxation at the nano sheets film interface. EDS analysis (Fig S5[63]) further confirmed the chemical composition of the films in atomic ratio of 21.83: 57.41: 20.76 for Zn: O: C respectively.

Resistivity values were determined by Van der Pauw method[38] using four probe apparatus employing spring loaded gold plated probes. Resistivity values obtained with different concentrations of GO are tabulated below. Increasing GO concentrations lowers the resistivity. We assume that graphene provided a two dimensional fast electron transport framework in the ZnO nanoparticles matrix. However, we could limit the concentration of GO to 0.6 vol% since higher concentrations resulted in films peeling off and greater restacking effects visible in the form of agglomerates on the surface, causing shortening of the devices.

Lead iodide forms a plate or needle like morphology as is evident from SEM micrographs in Fig. 3(a). This corresponds to the 2H polytype which is consistent with the earlier reports for such films formed by solution processing.[39] These films transform from needle like morphology to dense closely packed block like appearance for the $CH_3NH_3PbI_3$ crystals (Fig. 3(b), 3(c)), an indication of the preferential orientation of films along (110) plane, confirmed by XRD (Fig 4). This change in appearance is associated with the volume change upon intercalation of MAI in lead iodide crystal

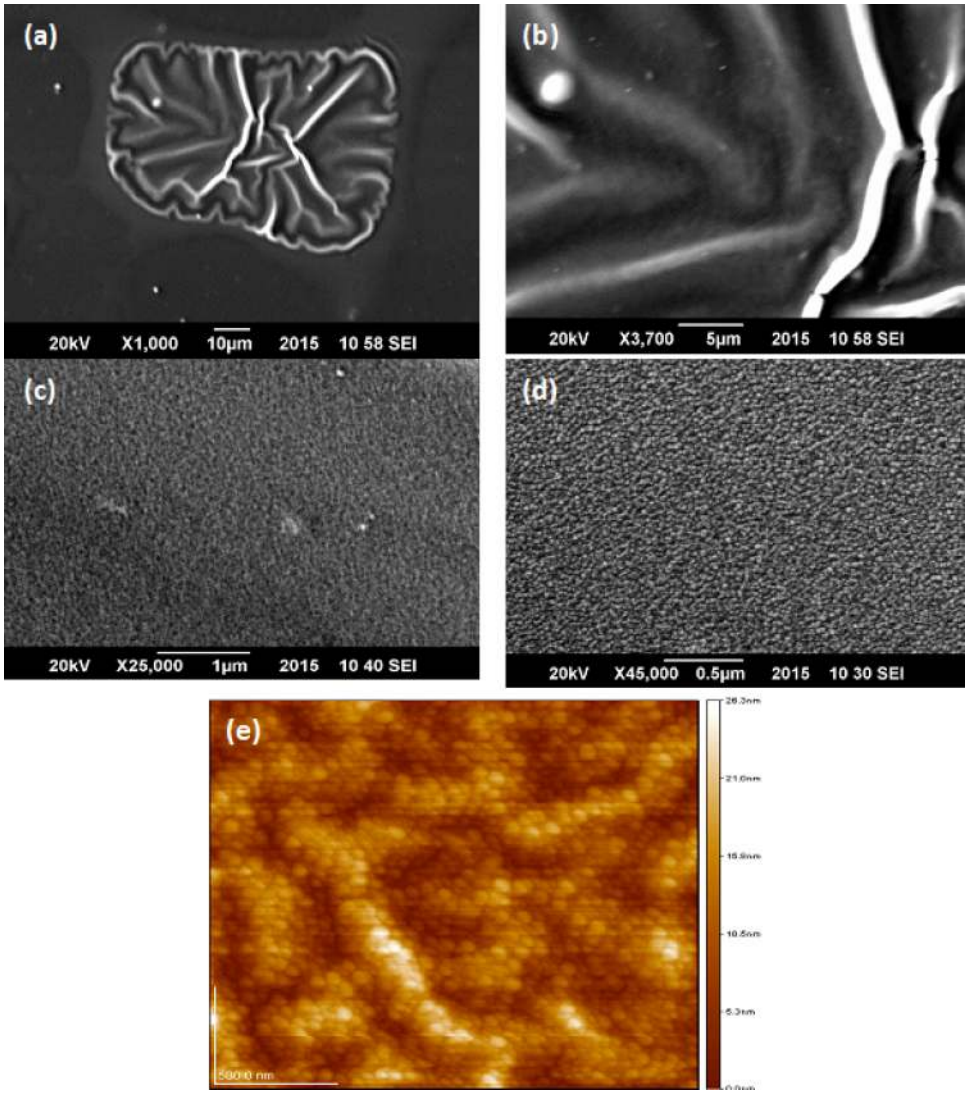

FIG. 2. (a, b, c, d) SEM micrographs of ZnO:GO films with increasing magnification illustrating imbedding of GO sheets in particle matrix and complete coverage of GO sheets by nanoparticles allowing effective 2-D charge transport highway. (e) AFM micrographs of ZnO:GO film.

structure.[40,41] Lead iodide has a unit volume of 124 $Å^3$ and upon reaction with MAI, unit volume changes to 990 $Å^3$ of $CH_3NH_3PbI_3$. Perovskite phase of $CH_3NH_3PbI_3$ consists of four units of $CH_3NH_3PbI_3$ in a unit cell so that the unit cell volume for this phase is 248 $Å^3$, almost twice that of lead iodide. This is the reason for the dense, blocky and rough appearance of the $CH_3NH_3PbI_3$ film under SEM.

Uniform film formation is manifested in low magnification, large area SEM images (Fig. 3(b), 3(c)), a proof of the efficiency of the synthesis protocol being developed for high humidity and ambient air conditions. An optimum humidity level during synthesis has been cited as the reason for superior optoelectronic and mass transport properties. Films thus grown were pin hole free while those grown under nitrogen filled environment presented non uniform morphology introducing extensive grain boundaries, a source of energetic disorder.[42] Larger grains with reduced grain boundaries were obtained when annealing operation was performed in air. It was postulated that humidity during annealing induces moisture assisted creep at grain boundaries resulting in improved carrier lifetimes.[42,43] Improved photovoltaic performance for these devices can also be attributed to additional charge carrier generation due to autoionization of adsorbed water molecules.

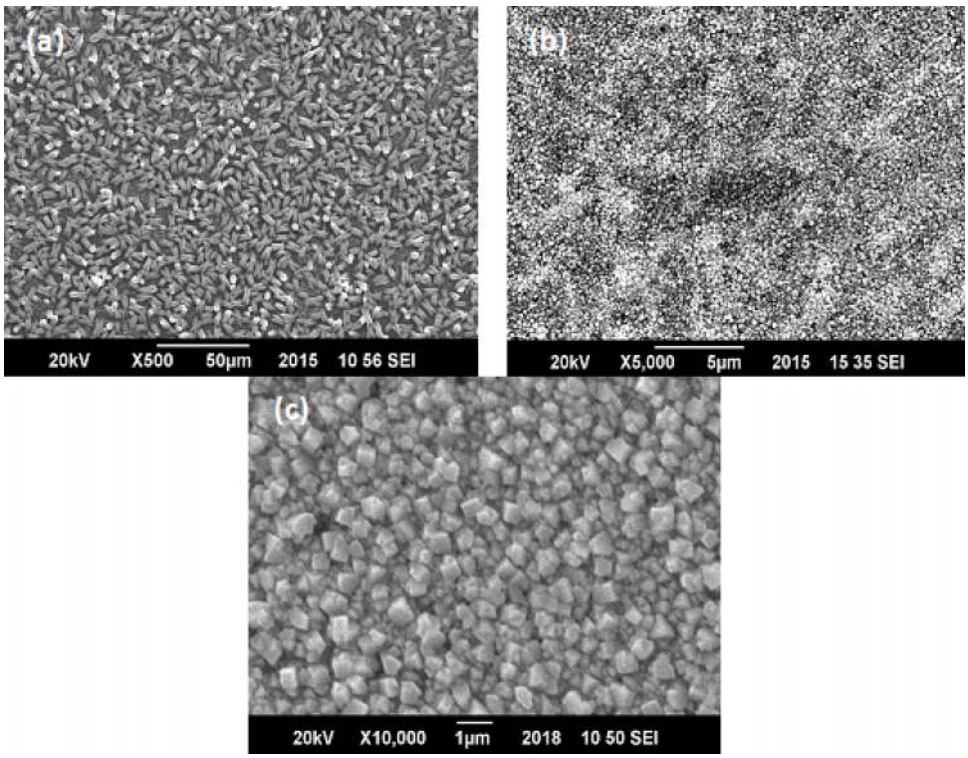

FIG. 3. (a) Low magnification SEM micrograph of lead idodide film showing complete coverage, (b, c) low and high magnification SEM micrographs of $CH_3NH_3PbI_3$ showing uniform large area complete coverage.

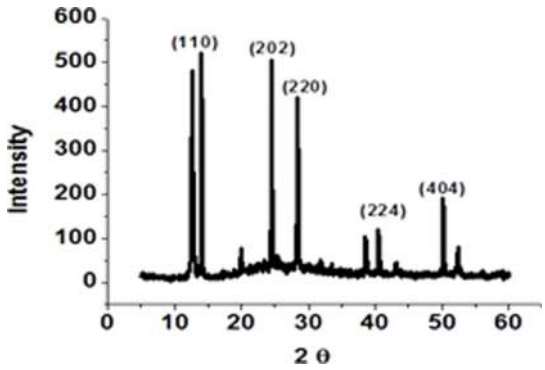

FIG. 4. XRD profile of $CH_3NH_3PbI_3$ films.

Autoionization creates surface OH^- species allowing protons to migrate between them generation additional charge carriers.

Diffraction pattern presented in Fig. 4 is found to be consistent with the tetragonal phase of the $CH_3NH_3PbI_3$ with sharp peaks at 14.0, 24.3, 28.4, 31.7, 40.5, 43.0, and 50.3°, corresponding planes have been indexed in Fig. 4.[39,44–46] Some residual lead iodide (JCPDS Card No. 07–0235) is also evident and is considered to be beneficial for the photovoltaic performance by improving carrier lifetime. This residual lead iodide at the grain boundaries is also attributed to reduced recombination at the absorber electron selective contact interface.

JV curves obtained for ZnO and ZnO-GO based devices are presented in Fig 5(a) along with tabulated performance parameters. The improved performance for ZnO-GO based devices is attributed to the inclusion of GO in ZnO films providing an additional favorable step in the energy

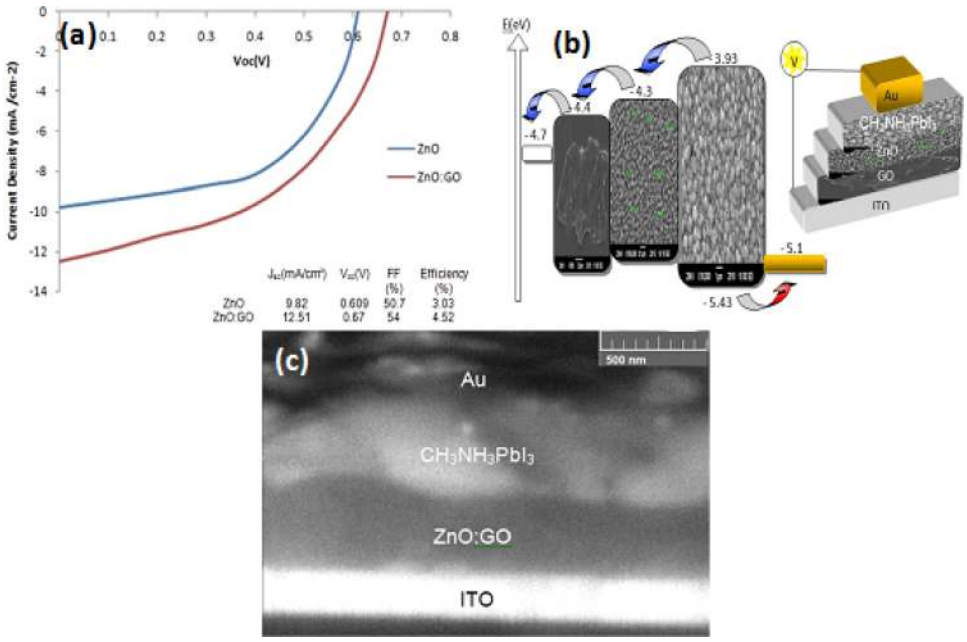

FIG. 5. (a) JV curve, (b) device schematic and energy level diagram and (c) device crosssection for the complete cell.

scheme (Fig. 5(b)). This two dimensional network of GO in the matrix provides higher charge transport, resulting in better electron collection and reduced interfacial resistance. Furthermore, it also affects the FF by reducing the series resistance of the complete device. Higher electron mobilities and better charge collection affects the space charge region at the interface, resulting in increase in device performance.

Relative electron affinities at the interfaces have profound effect on the impedance response. To have a quantitative evaluation of the improvement by addition of GO in ZnO matrix, impedance spectroscopy for the devices was performed. This is a versatile non destructive technique to evaluate the device physics, charge transport and recombination dynamics in solar cells, and has extensively been employed in the study of DSSCs.[47–51] Obtained data were modeled using an equivalent circuit using two RC components in parallel with a series resistance (Fig. 6). Rs is attributed to circuit wires and ITO while Rsc is attributed to selective contact and Rrec being the recombination resistance of the $CH_3NH_3PbI_3$ absorber. Constant phase elements were used instead of ideal capacitors for best data fit. Randomized with Levenberg-Marquardt fitting method was used with error defined at 10^{-6} for the data fitting operation at 100000 iterations. Nyquist plots, presented in Fig. 7, consist of a typical recombination arc at intermediate frequency with an additional low frequency arc.[52]

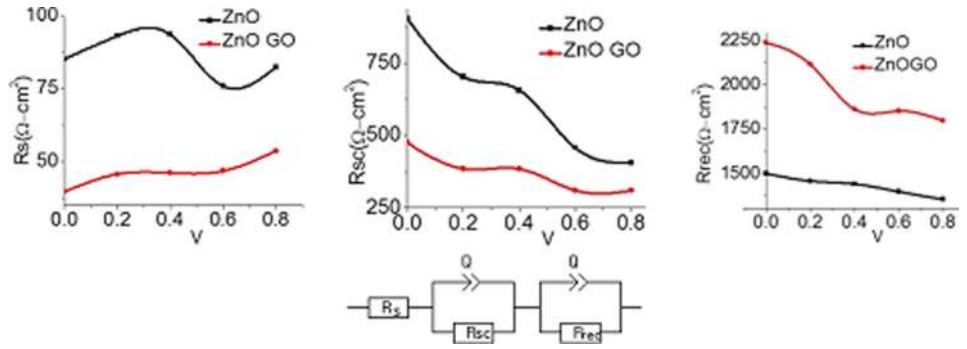

FIG. 6. R_s, R_{sc} and R_{rec} plots for ZnO and ZnO-GO based devices, with equivalent circuit.

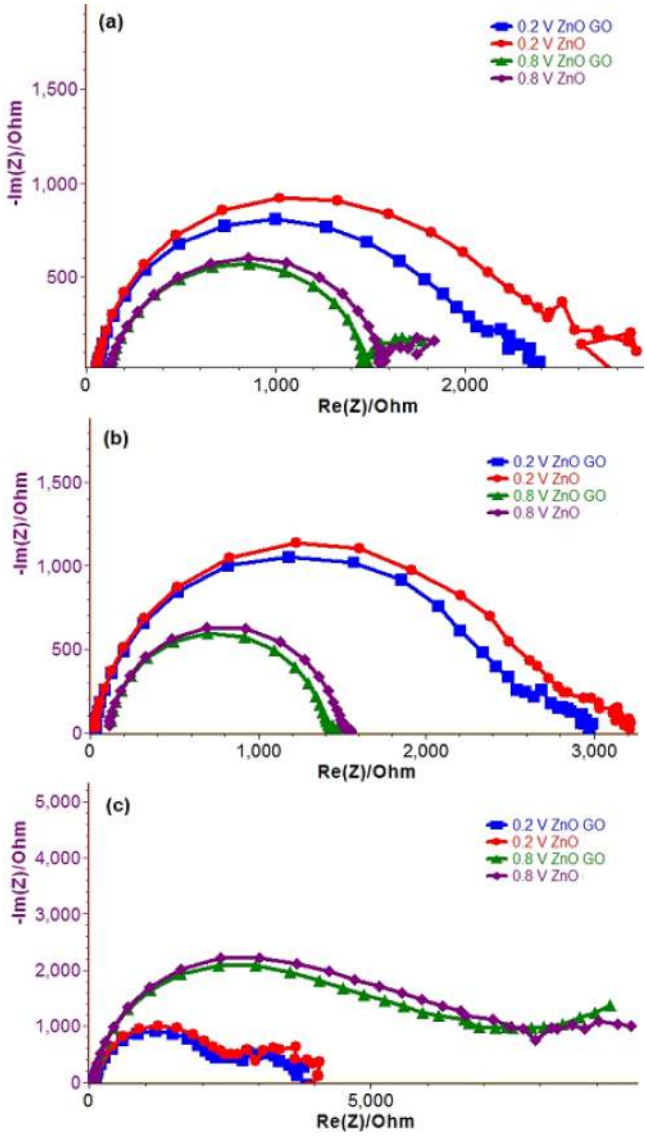

FIG. 7. Nyquist plots for TiO_2 and TiO_2-GO based device at 25 °C (a), 40 °C (b) and 60 °C (c).

Series resistance is a combination of Rs and Rsc[53] and a lower value of series resistance translate into higher value of FF. With the addition of GO, the series resistance decreases which is evident with an increase in the FF for the cells employing ZnO nanocomposite as electron selective contact (Fig. 6). Lower values of series resistance with addition of GO is due to the higher electron mobilities and lower resistivity values for the ZnO-GO nanocomposite. This lower value of series resistance can be a very important parameter for the optimization of these devices for commercial applications. For large areas of cells involved in commercial applications, any decrease in series resistance is highly desirable since small increase can have serious deleterious effects on the performance of large area photovoltaic modules.

Intermediate frequency feature in Nyquist plot contribute Rrec[53] and higher values of recombination resistance Rrec and a lower slope with increase in the applied bias voltage is reflective of higher open circuit voltage of the device. Charge carrier concentration in the absorber is directly proportional to the applied bias, higher concentrations with higher applied potentials and vice versa. This increasing concentration with applied bias results in decrease in Rrec with increasing applied

potential which corresponds to the increased recombination at the interfaces owing to the higher densities of the charge carriers.

Slope of Rrec plot is inversely proportional to the FF, higher slope of Rrec means lower value of FF and a lower slope of Rrec plot with increasing applied potential mean an increased FF. With the addition of GO, Rrec increases with a steady slope with increasing applied potential and is thus responsible for the increase of FF in the devices employing ZnO-GO nanocomposite as electron selective contact.

Low frequency feature is observed in the Nyquist plots as presented in Fig. 7. The origin of this low frequency feature is debated in literature. Few researchers assign it as having no bearing on the device physics and exclude it from data analysis[54] while other have identified this feature with a slower time constant for charge accumulation by ferroelectric domain walls.[55] Trap state distribution in $CH_3NH_3PbI_3$ has itself been attributed to this additional low frequency feature.[47] Low temperature synthesis processes involved results in higher densities of sub band gap trap states. Kinetics of trapping and release of charges at these sites could be the reason of this additional low frequency feature. Differences in electron affinities of the contacting interfaces have also been

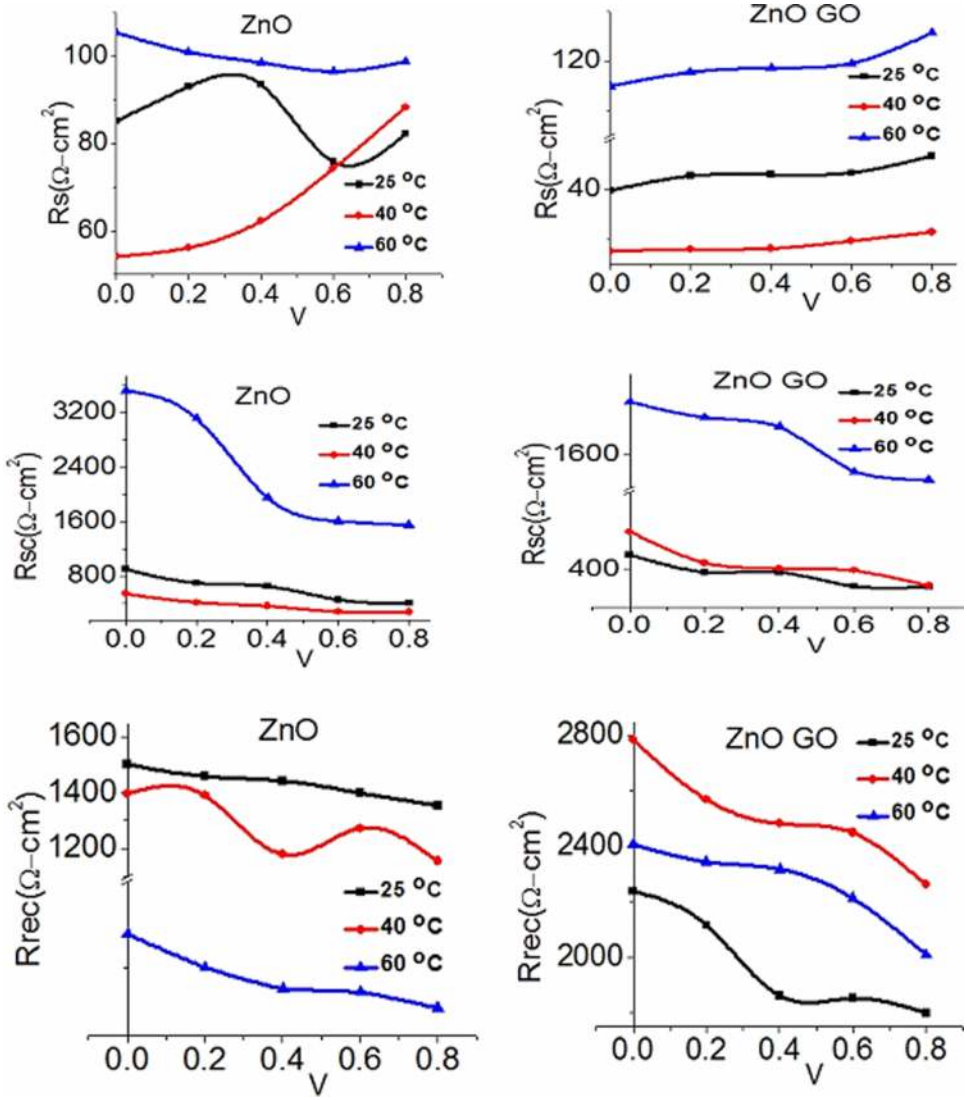

FIG. 8. Rs, Rsc and Rrec plots for ZnO and ZnO-GO based devices obtained at different temperatures. Legend along each plot indicates the test conditions.

attributed to be the source of this feature.[53] This low frequency feature is a characteristic for IS spectrum for DSSCs and has been attributed to the ionic mobility in the liquid electrolyte employed in the DSSCs. Recently ionic migration has been identified in $CH_3NH_3PbI_3$ absorber based devices[56,57] and can thus be the reason of this additional low frequency feature in Nyquist plots. Therefore we have included this feature in our curve fitting process.

Temperature induced physical processes can be evaluated by the study of impedance spectra obtained at elevated temperatures. To visualize the effect of temperature on the recombination and charge carrier dynamics at the interfaces and the bulk of the materials, we carried out IS measurements at the elevated temperatures of 40 °C and 60 °C. Nyquist plots obtained and the values for Rs, Rsc and Rrec are presented in Fig. 8. Value of Rs decreases with increase in the temperature up to 40 °C and that of Rrec increases, an indication of improved performance with a higher FF and Voc at this temperature. As the temperature is increased to 60 °C, there is an increase in series resistance and a sharp decrease in Rrec. Variation in the coefficients of thermal expansion of the materials at the interface can also affect the series resistance and the recombination rate. An increased density of defects at the interface can cause increased trap assisted recombination at the interface manifested with an increase in Rrec and series resistance.

Though the diffusion rate is expected to increase with increase in the temperature which should lower the series resistance component of the impedance response, our observations to the contrary can be attributed to the coefficient of thermal expansion mismatch between the contacting interfaces.[58] Quantitative evidence of the effect of increased temperatures on the contacting surfaces presented by Luis K. Ono *et al.*[59] prove that the τ_{fast} process play a dominant role in the device performance at elevated temperatures and are attributed to selective contacts. This mismatch affects the density of trap states at the interface and is bound to increase the recombination rate and is the source of increasing Rrec with temperature. Thus FF and Voc are expected to decrease with temperatures in the range of 60 °C. Phase change in $CH_3NH_3PbI_3$ at 55 °C[60] is also associated with increase in the Rrec with a lower Voc above this temperature.

We observed very low hysteresis for our devices (Fig. 9) which can be attributed to the very low resistivity of the ZnO-GO electron selective contact. Hysteresis effects have been associated with planer device geometry. Snaith and coworkers[61] postulated that contact resistance at the interface with electron selective contact can be identified as a possible source of this behavior and is the reason why mesoporous and mesosuperstructured scaffolds are relatively free of this phenomenon, since increased surface area facilitates greater electron uptake. Miyasaka and co workers[62] presented conclusive evidence identifying TiO_2 and its interface as the source of this hysteresis. Low electron mobilities of TiO_2 leads to charge build up at the interface and causes rate and scan direction dependent hysteresis. ZnO with its superior electron transport properties avoids this build up of charges by fast quenching of generated electrons in the absorbers. This is further improved by the addition of GO as is evident by the decrease in resistivity (Table I). Decrease in series resistance by the incorporation of highly conductive GO in ZnO matrix increases charge collection efficiency

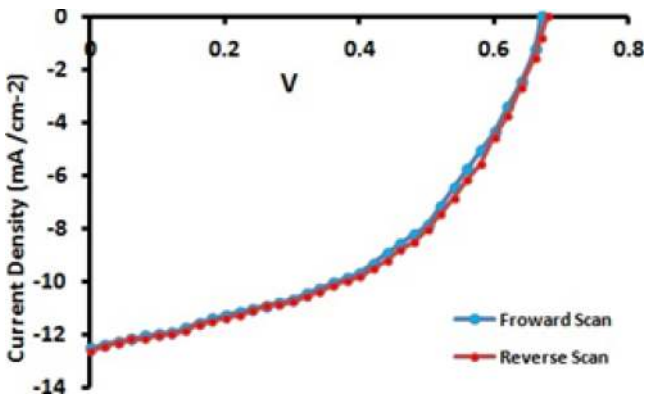

FIG. 9. Scan direction dependent J-V curves for solar cells based on ZnO-GO electron selective contacts.

TABLE I. Resistivity values of ZnO GO composites.

Sample	Resistivity (Ω m)
0 vol %	1.97×10^{2}
0.2 vol %	$6.70\text{x } 10^{-3}$
0.4 vol %	$4.61\text{x}10^{-3}$
0.6 vol %	$6.34\text{x}10^{-2}$
0.8 vol %	$1.94\text{x}10^{-2}$
1.0 vol %	$1.76\text{x}10^{-2}$

and results in very low hysteresis in these devices. Interfaces have also been identified as the source of this hysteresis[62] and the absence of HTL $CH_3NH_3PbI_3$ interface provides additional stabilization against this hysteresis effect.

V. CONCLUSIONS

We have demonstrated an HTL free device based on ZnO-GO nanocomposite electron selective contact. The processing was customized for ambient air conditions of high humidity with an improved efficiency from 3.02% for ZnO alone to 4.6% for the nanocomposite. The efficiency obtained may not be the best reported for this class of absorber but the device construction/architecture reported has the potential of reducing the material and processing cost of this technology by avoiding expensive HTL and avoiding processing under high vacuum environments. Furthermore, based on our experience with the device fabrication and its architecture, we propose that further increase in the efficiencies of such devices could be achieved by process optimizations and controlling the thickness of the individual layers involved.

ACKNOWLEDGMENTS

We thank staff at National Nanotechnology Research Centre Institute of Materials Science and Nanotechnology Bilkent University Turkey for help with J-V characterization. This research was funded by Higher Education Commission Pakistan through grant number 213-58732-2EG2-014(50023541).

[1] W. S. Yang *et al.*, "High-performance photovoltaic perovskite layers fabricated through intramolecular exchange," Science (80-.) **348**, 1234–1237 (2015).
[2] G. Xing *et al.*, "Long-range balanced electron- and hole-transport lengths in organic-inorganic CH3NH3PbI3," Science **342**, 344–7 (2013).
[3] S. D. Stranks *et al.*, "Electron-hole diffusion lengths exceeding 1 micrometer in an organometal trihalide perovskite absorber," Science **342**, 341–4 (2013).
[4] R. Sheng *et al.*, "Methylammonium Lead Bromide Perovskite-Based Solar Cells by Vapour-Assisted Deposition," J. Phys. Chem. C **119**, 150127132618007 (2015).
[5] H.-S. Kim, S. H. Im, and N.-G. Park, "Organolead Halide Perovskite: New Horizons in Solar Cell Research," J. Phys. Chem. C **118**, 5615–5625 (2014).
[6] J. Burschka *et al.*, "Tris(2-(1H-pyrazol-1-yl)pyridine)cobalt(III) as p-type dopant for organic semiconductors and its application in highly efficient solid-state dye-sensitized solar cells," J. Am. Chem. Soc. **133**, 18042–5 (2011).
[7] D. Bi *et al.*, "Using a two-step deposition technique to prepare perovskite (CH3NH3PbI3) for thin film solar cells based on ZrO2 and TiO2 mesostructures," RSC Adv. **3**, 18762 (2013).
[8] D. Bi, L. Yang, G. Boschloo, A. Hagfeldt, and E. M. J. Johansson, "Effect of Different Hole Transport Materials on Recombination in CH 3 NH 3 PbI 3 Perovskite-Sensitized Mesoscopic Solar Cells," J. Phys. Chem. Lett. **4**, 1532–1536 (2013).
[9] A. Mei *et al.*, "A hole-conductor-free, fully printable mesoscopic perovskite solar cell with high stability," Science (80-.) **345**, 295–298 (2014).
[10] S. Ye *et al.*, "CuSCN-based inverted planar perovskite solar cell with an average PCE of 15.6%," Nano Lett. 150504172654007 (2015), doi:10.1021/acs.nanolett.5b00116.
[11] H.-S. Ko, J.-W. Lee, and N.-G. Park, "15.76% Efficiency Perovskite Solar Cell Prepared under High Relative Humidity: Importance of PbI2 Morphology in Two-Step Deposition of CH3NH3PbI3," J. Mater. Chem. A **3**, 8808–8815 (2015).
[12] P. V. Kamat, "Quantum Dot Solar Cells. The Next Big Thing in Photovoltaics," J. Phys. Chem. Lett. **4**, 908–918 (2013).
[13] A. Kojima, K. Teshima, Y. Shirai, and T. Miyasaka, "Novel Photoelectrochemical Cell with Mesoscopic Electrodes Sensitized by Lead-halide Compounds (11)," Meet. Abstr. **MA2008-02**, 27 (2008).

[14] M. Law, L. E. Greene, J. C. Johnson, R. Saykally, and P. Yang, "Nanowire dye-sensitized solar cells," Nat. Mater. **4**, 455–9 (2005).
[15] C. Magne, T. Moehl, M. Urien, M. Grätzel, and T. Pauporté, "Effects of ZnO film growth route and nanostructure on electron transport and recombination in dye-sensitized solar cells," J. Mater. Chem. A **1**, 2079–2088 (2013).
[16] K. Mahmood, B. S Swain, and A. Amassian, "Double-layered ZnO nanostructures for efficient perovskite solar cells," Nanoscale **6**, 14674–8 (2014).
[17] E. Kymakis, E. Stratakis, M. M. Stylianakis, E. Koudoumas, and C. Fotakis, "Spin coated graphene films as the transparent electrode in organic photovoltaic devices," Thin Solid Films **520**, 1238–1241 (2011).
[18] G. Eda *et al.*, "Transparent and conducting electrodes for organic electronics from reduced graphene oxide," Appl. Phys. Lett. **92**, 233305 (2008).
[19] M. Khenfouch, M. Baïtoul, and M. Maaza, "White photoluminescence from a grown ZnO nanorods/graphene hybrid nanostructure," Opt. Mater. (Amst) **34**, 1320–1326 (2012).
[20] C. Zhu *et al.*, "One-pot, water-phase approach to high-quality graphene/TiO2 composite nanosheets," Chem. Commun. (Camb) **46**, 7148–50 (2010).
[21] X. Li *et al.*, "Synthesis of 3D Hierarchical Fe 3 O 4 /Graphene Composites with High Lithium Storage Capacity and for Controlled Drug Delivery," J. Phys. Chem. C **115**, 21567–21573 (2011).
[22] J. O. Hwang *et al.*, "Vertical ZnO nanowires/graphene hybrids for transparent and flexible field emission," J. Mater. Chem. **21**, 3432–3437 (2011).
[23] Z. Chen, N. Zhang, and Y.-J. Xu, "Synthesis of graphene–ZnO nanorod nanocomposites with improved photoactivity and anti-photocorrosion," CrystEngComm **15**, 3022 (2013).
[24] G. Williams and P. V. Kamat, "Graphene-semiconductor nanocomposites: excited-state interactions between ZnO nanoparticles and graphene oxide," Langmuir **25**, 13869–73 (2009).
[25] J. T.-W. Wang *et al.*, "Low-temperature processed electron collection layers of graphene/TiO2 nanocomposites in thin film perovskite solar cells," Nano Lett. **14**, 724–30 (2014).
[26] G. S. Han *et al.*, "Reduced Graphene Oxide/mesoporous TiO2 Nanocomposite based Perovskite Solar Cells," ACS Appl. Mater. Interfaces **7**, 151007124925005 (2015).
[27] X. Dong, H. Hu, B. Lin, J. Ding, and N. Yuan, "The effect of ALD-Zno layers on the formation of CH3NH3PbI3 with different perovskite precursors and sintering temperatures," Chem. Commun. (Camb) **50**, 14405–8 (2014).
[28] J. Dong *et al.*, "Impressive enhancement in the cell performance of ZnO nanorod-based perovskite solar cells with Al-doped ZnO interfacial modification," Chem. Commun. (Camb) **50**, 13381–4 (2014).
[29] X. Xu *et al.*, "Highly efficient planar perovskite solar cells with a TiO 2 /ZnO electron transport bilayer," J. Mater. Chem. A **3**, 19288–19293 (2015).
[30] S. Salam, M. Islam, and A. Akram, "Sol–gel synthesis of intrinsic and aluminum-doped zinc oxide thin films as transparent conducting oxides for thin film solar cells," Thin Solid Films **529**, 242–247 (2013).
[31] W. H., Jr. and R. Offeman, "Preparation of graphitic oxide," J. Am. Chem. . . . (1958).
[32] A. Lerf, H. He, M. Forster, and J. Klinowski, "Structure of Graphite Oxide Revisited ‖," J. Phys. Chem. B **102**, 4477–4482 (1998).
[33] C. Zhang *et al.*, "Facile synthesis and strongly microstructure-dependent electrochemical properties of graphene/manganese dioxide composites for supercapacitors," Nanoscale Res. Lett. **9**, 490 (2014).
[34] D. Li, M. B. Müller, S. Gilje, R. B. Kaner, and G. G. Wallace, "Processable aqueous dispersions of graphene nanosheets," Nat. Nanotechnol. **3**, 101–5 (2008).
[35] A. Yu, P. Ramesh, M. E. Itkis, E. Bekyarova, and R. C. Haddon, "Graphite Nanoplatelet-Epoxy Composite Thermal Interface Materials," J. Phys. Chem. C **111**, 7565–7569 (2007).
[36] X. Yang, J. Zhu, L. Qiu, and D. Li, "Bioinspired effective prevention of restacking in multilayered graphene films: towards the next generation of high-performance supercapacitors," Adv. Mater. **23**, 2833–8 (2011).
[37] Y. Wang *et al.*, "Preventing Graphene Sheets from Restacking for High-Capacitance Performance," J. Phys. Chem. C **115**, 23192–23197 (2011).
[38] 1958 Van Der Pauw (Philips Res Rep) a Method of Measuring Specific Resistivity and Hall Effect of Discs of Arbitrary Shape.
[39] J. Burschka *et al.*, "Sequential deposition as a route to high-performance perovskite-sensitized solar cells," Nature **499**, 316–9 (2013).
[40] D. Liu, M. K. Gangishetty, and T. L. Kelly, "Effect of CH 3 NH 3 PbI 3 thickness on device efficiency in planar heterojunction perovskite solar cells," J. Mater. Chem. A **2**, 19873–19881 (2014).
[41] Q. Chen *et al.*, "Planar heterojunction perovskite solar cells via vapor-assisted solution process," J. Am. Chem. Soc. **136**, 622–5 (2014).
[42] J. You *et al.*, "Moisture assisted perovskite film growth for high performance solar cells," Appl. Phys. Lett. **105**, 183902 (2014).
[43] H. Zhou *et al.*, "Interface engineering of highly efficient perovskite solar cells," Science (80-.) **345**, 542–546 (2014).
[44] J.-Y. Jeng *et al.*, "CH3NH3PbI3 perovskite/fullerene planar-heterojunction hybrid solar cells," Adv. Mater. **25**, 3727–32 (2013).
[45] H.-B. Kim *et al.*, "Mixed solvents for the optimization of morphology in solution-processed, inverted-type perovskite/fullerene hybrid solar cells," Nanoscale **6**, 6679–83 (2014).
[46] O. Malinkiewicz *et al.*, "Perovskite solar cells employing organic charge-transport layers," Nat. Photonics **8**, 128–132 (2013).
[47] L. Bertoluzzi, P. P. Boix, I. Mora-Sero, and J. Bisquert, "Theory of Impedance Spectroscopy of Ambipolar Solar Cells with Trap-Mediated Recombination," J. Phys. Chem. C **118**, 16574–16580 (2014).
[48] F. Fabregat-Santiago, J. Bisquert, G. Garcia-Belmonte, G. Boschloo, and A. Hagfeldt, "Influence of electrolyte in transport and recombination in dye-sensitized solar cells studied by impedance spectroscopy," Sol. Energy Mater. Sol. Cells **87**, 117–131 (2005).

[49] I. Mora-Seró, G. Garcia-Belmonte, P. P. Boix, M. A. Vázquez, and J. Bisquert, "Impedance spectroscopy characterisation of highly efficient silicon solar cells under different light illumination intensities," Energy Environ. Sci. **2**, 678 (2009).
[50] I. Mora-Seró *et al.*, "Recombination rates in heterojunction silicon solar cells analyzed by impedance spectroscopy at forward bias and under illumination," Sol. Energy Mater. Sol. Cells **92**, 505–509 (2008).
[51] J. Bisquert, E. Palomares, and C. A. Quiñones, "Effect of energy disorder in interfacial kinetics of dye-sensitized solar cells with organic hole transport material," J. Phys. Chem. B **110**, 19406–11 (2006).
[52] F. Fabregat-Santiago, G. Garcia-Belmonte, I. Mora-Seró, and J. Bisquert, "Characterization of nanostructured hybrid and organic solar cells by impedance spectroscopy," Phys. Chem. Chem. Phys. **13**, 9083–118 (2011).
[53] E. J. Juarez-Perez *et al.*, "Role of the Selective Contacts in the Performance of Lead Halide Perovskite Solar Cells," J. Phys. Chem. Lett. **5**, 680–5 (2014).
[54] H.-S. Kim *et al.*, "High efficiency solid-state sensitized solar cell-based on submicrometer rutile TiO2 nanorod and CH3NH3PbI3 perovskite sensitizer," Nano Lett. **13**, 2412–7 (2013).
[55] R. S. Sanchez *et al.*, "Slow Dynamic Processes in Lead Halide Perovskite Solar Cells. Characteristic Times and Hysteresis," J. Phys. Chem. Lett. **5**, 2357–2363 (2014).
[56] C. Eames *et al.*, "Ionic transport in hybrid lead iodide perovskite solar cells," Nat. Commun. **6**, 7497 (2015).
[57] E. L. Unger *et al.*, "Hysteresis and transient behavior in current-voltage measurements of hybrid-perovskite absorber solar cells," Energy Environ. Sci. **7**, 3690–3698 (2014).
[58] L. Cojocaru *et al.*, "Temperature Effects on the Photovoltaic Performance of Planar Structure Perovskite Solar Cells," Chem. Lett. 1557 (2015), doi:10.1246/cl.150781.
[59] L. K. Ono, S. R. Raga, S. Wang, Y. Kato, and Y. Qi, "Temperature-dependent hysteresis effects in perovskite-based solar cells," J. Mater. Chem. A **3**, 9074–9080 (2014).
[60] C. Quarti *et al.*, "Structural and Optical Properties of Methylammonium Lead Iodide Across the Tetragonal to Cubic Phase Transition: Implications for Perovskite Solar Cells," Energy Environ. Sci. (2015), doi:10.1039/C5EE02925B.
[61] H. J. Snaith *et al.*, "Anomalous Hysteresis in Perovskite Solar Cells," J. Phys. Chem. Lett. **5**, 1511–1515 (2014).
[62] A. K. Jena *et al.*, "The Interface between FTO and TiO2 Compact Layer can be one of the Origins to Hysteresis in Planar Heterojunction Perovskite Solar Cells," ACS Appl. Mater. Interfaces **7**, 9817–9823 (2015).
[63] See supplementary material at http://dx.doi.org/10.1063/1.4953397 for effects of processing condition on morphology of $CH_3NH_3PbI_3$ films and roughness profiles of $CH_3NH_3PbI_3$ and ZnO-GO films. Also included is the optical profilometer thickness profile for ZnO films used for resistivity measurements and EDS data for ZnO-GO nanocomposite.